


2011-01-01

Fabrication And Characterization Of Nanocrystalline Yttrium Oxide Thin Films For Electronic Device Applications

Mudavakkat Vikas Haridas

University of Texas at El Paso, haridas.vikas@gmail.com

Follow this and additional works at: https://digitalcommons.utep.edu/open_etd

 Part of the [Electrical and Electronics Commons](#), [Materials Science and Engineering Commons](#), and the [Mechanics of Materials Commons](#)

Recommended Citation

Vikas Haridas, Mudavakkat, "Fabrication And Characterization Of Nanocrystalline Yttrium Oxide Thin Films For Electronic Device Applications" (2011). *Open Access Theses & Dissertations*. 2409.
https://digitalcommons.utep.edu/open_etd/2409

This is brought to you for free and open access by DigitalCommons@UTEP. It has been accepted for inclusion in Open Access Theses & Dissertations by an authorized administrator of DigitalCommons@UTEP. For more information, please contact lweber@utep.edu.

FABRICATION AND CHARACTERIZATION OF NANOCRYSTALLINE YTTRIUM
OXIDE THIN FILMS FOR ELECTRONIC DEVICE APPLICATIONS

MUDAVAKKAT VIKAS HARIDAS, B.S.C.S

Department of Electrical and Computer Engineering

APPROVED:

C. V. Ramana, Ph.D., Chair

Joseph Pierluissi, Ph.D.

Thompson Sarkodie-Gyan, Ph.D.

Yirong Lin, Ph. D.

Benjamin C. Flores, Ph.D.
Acting Dean of the Graduate School

FABRICATION AND CHARACTERIZATION OF NANOCRYSTALLINE YTTRIUM
OXIDE THIN FILMS FOR ELECTRONIC DEVICE APPLICATIONS

By

MUDAVAKKAT VIKAS HARIDAS, B.S.C.S

THESIS

Presented to the Faculty of Graduate School of
The University of Texas at El Paso
in Partial Fulfillment
of the Requirements
for the Degree of

MASTER OF SCIENCE

Department of Electrical and Computer Engineering

UNIVERSITY OF TEXAS AT EL PASO

DECEMBER 2011

ACKNOWLEDGEMENTS

I would like to first thank my advisor Dr. C.V Ramana for allowing me to be part of his ever growing research team and for his unwavering support through thick and thin. His passion and dedication to his research lit the same drive in me to pursue this research topic, which at first seemed like a tough nut to crack. Even when things looked bleak due to circumstances outside our control he has been always positive and supportive of my efforts. And as a result we have had some excellent data to publish and push forward this research avenue.

Special thanks to Dr. Kamala Bharathi, who during his time at UTEP helped me immensely in understanding formulae, the science and technical jargon of this research area. He has on many occasions helped me get through analyzing and organizing the data acquired through various sample characterization processes.

I thank my parents and my sister for their patience in allowing me to complete my thesis as it is always hard to wait on your child to see them succeed and prosper with a means to make living soon after university.

I also take this opportunity to thank my close friends on the UTEP campus Chandra Sekhar Papu, Nagendra Kiran Kambhampati, Praveen Palakurthi and Mohammed Alkhatib. They have been there to give me advice and give me company during our late nights at the labs when I worked on my thesis draft. Not to forget the refreshing rounds of Halo we played to get our batteries recharged.

At work I have to thank my boss Mr. Jose Luis Munoz for his support and understanding when I showed up late after staying up all night in the labs, he is another one of my best buddies at UTEP. I also thank Mr. Leo Saldivar and Mr. Oscar Prieto for their support and company.

And finally I wish to thank Jenni Wong, who is someone very important in my life, for giving me the moral support and keeping me cheered up when things weren't going well with my depositions.

ABSTRACT

This thesis presents the optimization of growth conditions for fabricating nanocrystalline Yttrium Oxide (Y_2O_3) thin films on silicon and optical grade, high quality quartz substrates in order to study its structural, optical and electrical properties for electronic device applications.

Commercially Y_2O_3 has proven to be difficult to fabricate at high quality due to its high temperature growth requirements and the need to alter established fabrication methods for electronic devices. A high temperature requirement for high quality poses a problem for research and analysis. This calls upon for an optimization of the growth conditions to facilitate fabrication of thin films for study that does not require mass production level efficiency or material growth speed. The work in thesis research started out with basic parameters used in industry for growth conditions despite having varying deposition methods and equipment that were used in the existing literature.

Reducing the chamber pressure while maintaining the argon to oxygen ratio improved the Y-oxide film quality; lower deposition pressures afford higher deposition rates of material onto the substrates. Once promising samples were obtained, the chamber pressures were lowered to the least possible values at which an ignited plasma was sustainable while still maintaining constant argon to oxygen ratio.

The effect of processing conditions on the structure, optical and electrical properties demonstrated that the approach is viable and yielded fairly good quality Y_2O_3 thin films. The quality of the samples was evident from the observed high refractive index at high temperatures, good electrical properties and excellent stoichiometry. These samples proved that optimizations of growth conditions can be made such that high temperatures were not required to fabricate

samples to study the properties of the material. It also showed promise for commercial level optimizations that may lead to lower demands of higher temperatures for mass production.

TABLE OF CONTENTS

	Pages
ACKNOWLEDGEMENTS	iii
ABSTRACT	v
TABLE OF CONTENTS.....	vii
LIST OF FIGURES	ix
CHAPTER 1: THESIS CHALLENGES AND MOTIVATION.....	1
1.1 Introduction	1
1.2 Developments	3
1.3 Candidate material:.....	6
CHAPTER 2: THIN FILMS	9
2.1 History	9
2.2 Developments until the present	10
CHAPTER 3: CONCEPT OF SPUTTERING	12
3.1 Definition	12
3.2 Basic working	12
3.3 Magnetron Sputtering	13
3.4 RF Magnetron Sputtering.....	14
CHAPTER 4: EXPERIMENTAL	16
4.1 Preparation	16
4.2 Equipment.....	17
4.3 Deposition procedure	18
4.4 Shutdown	19
4.5 Characterization	20
CHAPTER 5: RESULTS AND DISCUSSION.....	22
5.1 Structure and growth behavior.....	22
5.2 Chemical Composition	26
5.3 Optical Constants	30
5.4 Electrical Characteristics	36
CHAPTER 6: CONCLUSIONS	41
REFERENCES	42

CURRICULUM VITAE.....	46
-----------------------	----

LIST OF FIGURES

Figure 1. Standard Transistor model with SiO ₂ as gate oxide material.....	1
Figure 2. SEM cross section of gate oxide layer at 90nm ^[55]	2
Figure 3. HK-MG Transistor model proposed in general	3
Figure 4. IBM/AMD's FinFET Transistor model	5
Figure 5. Intel's 3D Transistor Model	6
Figure 6. The working of R.F Magnetron Sputtering system	15
Figure 7. XRD patterns of Y ₂ O ₃ films grown on Si(100) substrates	22
Figure 8. RHEED patterns of Y ₂ O ₃ films	24
Figure 9. Variation of grain size of Y ₂ O ₃ films with growth temperature	25
Figure 10. RBS spectra of Y ₂ O ₃ films grown at various temperatures	27
Figure 11. The atomic ratio of oxygen to yttrium in Y ₂ O ₃ films grown at various temperatures.....	29
Figure 12. The spectral dependence of Ψ and Δ for Y ₂ O ₃ films	31
Figure 13. The spectral dependence of k for Y ₂ O ₃ films as a T _s	32
Figure 14. The spectral dependence of the index of refraction (n) of Y ₂ O ₃ films as a function of growth conditions.....	34
Figure 15. Variation of the electrical conductivity of Y ₂ O ₃ with T _s	36

Figure 16. Frequency dependent conductivity of Y_2O_3 37

Figure 17. (a) Variation of the mean relaxation time (τ); (b) the spreading factor (α) with increasing T_s .. 39

CHAPTER 1: THESIS CHALLENGES AND MOTIVATION

1.1 Introduction

The ASIC (application-specific integrated circuit) and COTS (commodity of the shelf) chips of today are striving to offer the best in performance-to-watt ratios.^[1] This should come as no surprise as the grandiose statements by Intel, during the launch of its Pentium 4 processor, of 15 Ghz chips by the year 2010 have failed to materialize.^[1] Granted they did demonstrate an ALU (arithmetic logic unit) running at 10ghz^[3], it was still a far cry from a full blown commercial CPU. Intel, AMD and the others all soon ran into the infamous frequency barrier. The distinctive inability to clock the CPUs any higher than the 4 Ghz mark without having the thermal envelopes sky rocketing. The culprit was the enormous leakage current. Silicon Dioxide (SiO_2) based gate oxides for transistors were reaching their limits in preventing leakage current in chips even during idle modes or off modes.^[4] Figure 1 shows the standard transistor model.

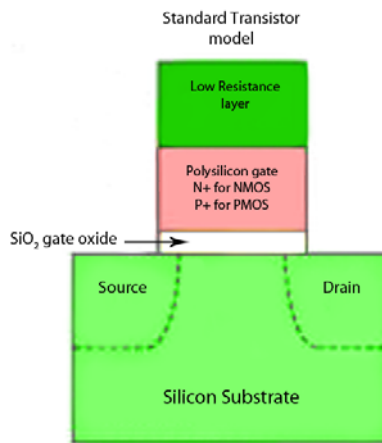


Figure 1. Standard Transistor model with SiO_2 as gate oxide material

Operational voltage V_{dd} has been scaling down with the scaling down of the channel width which helps keep power envelopes in check. But as a consequence gate oxide thicknesses were also getting reduced. On the 90 nm process Intel reported a gate oxide thickness of 1.2 nm or 12 Å as shown in Figure 1, this represents a layer that is no more than 4 atoms thick.^[5] This compounds the already identified weakness of SiO₂ based CMOS devices in combating leakage currents. High performance chip manufacturers were simply running out atoms to make up the gate oxide layer. The threshold voltage has to be accordingly compensated and scaled to match high performance requirements but undesirably sub threshold leakage current also increases as a result.^[6]

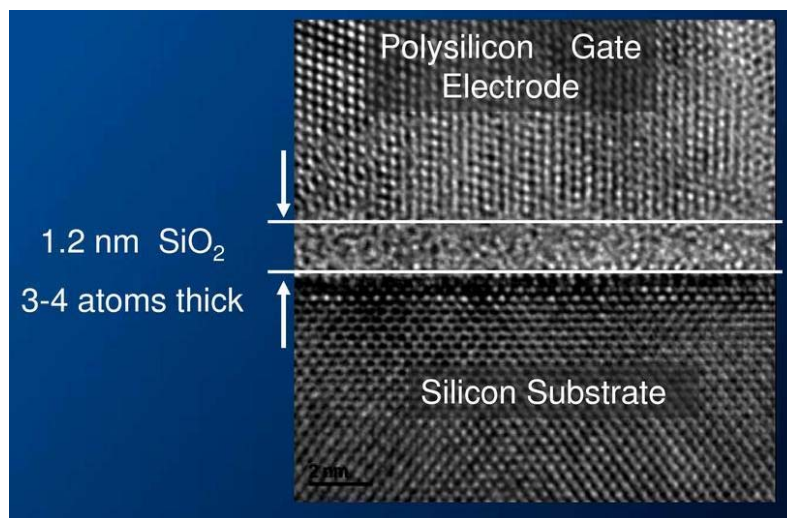


Figure 2. SEM cross section of gate oxide layer at 90nm^[55]

This setback resulted in the quest for increase computing capacity whilst maintaining the highest clock speeds possible within a fixed thermal envelope. When the first dual core CPUs were introduced the market started the bandwagon on multithreaded chips and applications as the next greatest step in computing progress. Commercial CPUs started gaining ground as affordable

HPC (high performance computing) alternatives but power consumption remained a key issue. It was at this time the industry started to look towards alternatives to SiO_2 as a gate oxide.

1.2 Developments

Intel first introduced a hafnium based material (exact composition a corporate secret) as their choice High-K (high dielectric) material for their High-K Metal gate transistor technologies. The introduction was on their 45nm process with Hf based gate oxide as the 'high-K' while replacing the polysilicon electrode with metal base forming the 'Metal gate'. The HK-MG transistor model is as shown in Figure 3.

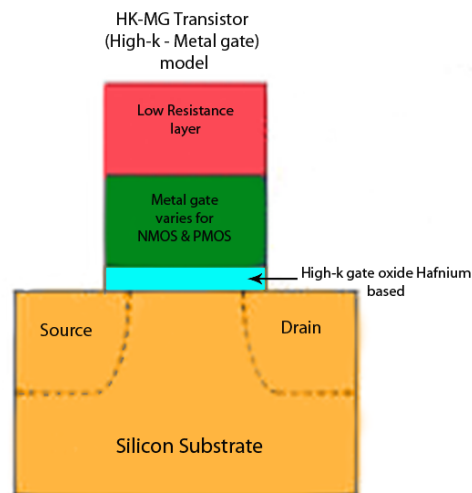


Figure 3. HK-MG Transistor model proposed in general

Intel reported transistor switching power to be reduced by as much as 30%, while still obtaining a performance improvement of as much as 20%, while gate current leakage reducing by a factor of 10. ^[7]

Silicon dioxide has served well at processes larger than 45 nm but as they get smaller than 65 nm as Intel explained, the transistor gate dielectric layer naturally becomes thinner. Up to 65 nm, this hasn't posed a problem; the thinner gate has led to an increase in the gate field effect, which is desirable. But with time a depletion region emerges between the gate and the electrode, in effect thickening the gate area, increasing the level of current necessary to implement a switch and there by degrading the overall "on" current.

Replacing SiO_2 with the hafnium based compound allowed Intel to go ahead and thicken the gate layer, therefore increasing the amount of "on" current. The electrode depletion issues were fixed with by replacing the polysilicon with a metal electrode.^[7]

While Intel kept the exact dielectric constants a trade secret, Hafnia or HfO_2 has a dielectric constant of 25 in comparison to that of SiO_2 at 3.9.^[8] It is widely assumed Intel used some form of hafnium silicate or hafnium oxide for high-K material.

Leaky transistors are easier to clock higher for pure speed at the expense of power efficiency and higher heat output. While more power efficient transistors become ideal candidates for slower speed operations. By utilizing this aspect of varying transistor properties through the manipulation of high-K materials used, ASIC chip makers like Nvidia were able to use slower transistors in section where pure speed was not important and then use leaky but faster transistors where outright faster switching speeds were desirable. The initial gains by this method on power draw were substantial while performance increased by virtue of new architectural gains. This led to the fierce competition between chip makers the world over in the budding field of lower power ASIC/COTS chip designs.

While consumers in the regular market pay lesser attention to the power consumption issues as long as the performance was top notch, HPC communities running larger server farms see the monetary savings and gains in space efficiency of having power efficient yet powerful chips. Marketing tactics no longer involves bombastic claims on performance increase alone. The focus now lies in the new concept of Performance per watt. The green revolution has not left its touch unfelt. More and more corporations requiring large compute farms are looking towards packing the most amount of processing power in the least of space with the lowest numbers on power consumption. Government initiatives to reward companies who can show improved power efficiencies year after year stand to enjoy tax cuts and other monetary benefits.^[9]

Recent announcements of the FinFET by IBM/AMD (Figure 4) and 3D Transistor concepts by Intel (Figure 5) highlights the growing challenges to maintaining transistor efficiency to clock high and increase cores per die whilst maintaining leakage at the lowest possible. 22 nm chips from Intel will see the introduction of the much trumpeted 3D transistors, which are actually similar to AMD's tri-gate transistor concept they announced some years ago. But whilst being based off hafnium based alloys and oxides, their potential viability in the high performance commodity CPUs is only for the short term, calling for even better materials to augment Hafnium based materials and possibly replace SiO_2 completely from all chip design markets in the near future.

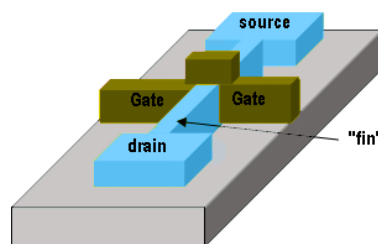


Figure 4. IBM/AMD's FinFET Transistor model

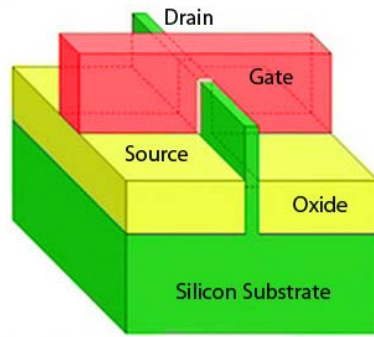


Figure 5. Intel's 3D Transistor Model

This motivation has led to the relentless research into materials that have very high dielectric constants in-order to aid the transistor technology's evolution into the coming decade. One such material marked out for research is Yttrium oxide (Y_2O_3). Yttrium oxide has demonstrated some interesting properties that could help the industry make even more significant gains in the coming years.

1.3 Candidate material:

Hafnium based materials made big waves in the industry with the first practical use in replacing SiO_2 as the gate oxide and the polysilicon electrodes on the 45 nm width channel transistors. Gains in the order of 100 times power consumption reduction were reported. However several other materials had already been identified prior to hafnium's commercial introduction. Amongst which included materials like zirconium dioxide (ZrO_2), Yttrium oxide (Y_2O_3), Lanthanum oxide (La_2O_3) and titanium dioxide (TiO_2).^[10] However materials like Y_2O_3 were not ready yet for mass commercial development. The process of its fabrication was still being fine tuned to practical levels for industry to seriously consider this an alternative to SiO_2 , though the

promising properties of this material ensured thorough explorations into ways of exploiting its advantages.

Several factors are to be considered when making such significant changes at the gate oxide level when it comes to mass production for commercial applications.

- 1) Replace the gate dielectric stack with the new materials discussed, but at the same time introducing minimal process changes; or
- 2) Replace the gate dielectric stack, and make substantial process changes to reduce process temperatures, but still retain the present CMOS device; or
- 3) Change the device geometry, structure and process, but retain the current materials; or
- 4) Introduce entirely new device mechanisms, for example, using alternative physical principles.^[10]

The above scenarios are key to the success of accepting a new material to replace SiO₂ as a gate oxide, as merely interesting properties might not prove commercially compelling for the industry.

Y₂O₃ films exhibit excellent electronic properties such as transparency over a broad spectral range 0.2–8 μm, high dielectric constant 14–18, high refractive index ~2, large band gap 5.8 eV, low absorption from near-UV to IR, and superior electrical breakdown strength 3 MV/cm.^[11-25]

Data stored in regular flash memory devices degrade over extended periods of time. Yttrium oxide based flash memory studies have shown improved data retention capabilities beyond that of regular flash memory devices^[26]. Such properties given the high dielectric constant make Y₂O₃ one of the best candidates to be seriously given consideration for commercial applications.

The optimal way to study such target materials is through thin film analysis for electrical, optical and mechanical properties. In this research work, we investigate these properties based on controlled growth of Y_2O_3 oxide layers on carefully chosen substrates to understand the relationship between growth factors. Such insight can lead to growth condition optimization with commercial applications in mind.

CHAPTER 2: THIN FILMS

Thin films are thin material layers ranging from fractions of a nanometer (known also as monolayer) to several micrometers in thickness. They are used in a myriad of applications from enhancing optical properties of lens (near ideal transparency). There are huge application for anti-reflective coatings which is a highly desirable trait for special camera lens and automobile windscreens. Beam splitters are derived by carefully formulated thin films that display high absorption rates facilitating in highly abrasive resistant coats for sunglass or windscreens. In the aerospace & military, applications for high temperature and durability coats are on the rise. Advanced process of delivering drugs to the systemic circulation via a thin film that dissolves when in contact with liquid is yet another revolution in its own right. These are some of the many applications that demonstrate the potential and value in research into thin films' in today's world.

2.1 History

The technology behind thin films would not be possible without the advancements in other areas as far back as 1640s when the first piston type vacuum pump was invented by Otto van Guericke to pump water out of mines. Following which was the first use of a vacuum pump to form a glow discharge (plasma) in a "vacuum tube" through Michael Faraday's effort in 1838. At the time he used brass electrodes and a vacuum of approximately 2 Torr. The history of thin films dates back to the mid 1800s when William Robert Grove was the first to study what would soon be known as "sputtering" although other inventors had observed the effect while studying glow discharges.

Later Thomas Edison filed a patent for application for a vacuum coating equipment to deposit coatings on his wax cylinder phonographs before subsequent electroplating. ^[27]

Technology has come far since the days of these rudimentary forms of thin film deposition, as the demands for faster, more even and precise depositions of various types of source materials gained traction. There are various methods to thin film depositions today and they maybe loosely referred to as Physical vapor deposition processes (PVD)

2.2 Developments until the present

After Thomas Edison's endeavors PVD methods have improved in the following route of increasing novelty:

Evaporative deposition: The material to be deposited is heated to a high vapor pressure by electrically resistive heating in "low" vacuum.

Electron beam PVD: The material to be deposited is heated to a high vapor pressure by electron bombardment in "high" vacuum.

Sputter deposition: A glow plasma discharge bombards the material sputtering some away as a vapor. When localized around the "target" by a magnet, it is called Magnetron sputtering.

Cathodic Arc Deposition: A high power arc directed at the target material blasts away some into a vapor.

Pulsed laser deposition (PLD): A high power laser ablates material from the target into a vapor.

Over the years Magnetron sputtering and PLD process have gained prominence with the industry. The deposition process used in this thesis work is the RF magnetron sputtering. It is therefore important to know the history behind the concept of sputtering and its development through history into its current form today.

CHAPTER 3: CONCEPT OF SPUTTERING

3.1 Definition

Sputtering is a process whereby atoms are ejected from a solid target material due to bombardment of the target by energetic particles ^[28].

3.2 Basic working

Sputtering operates with the aid of plasma. Plasma can be defined as the 4th state of matter where the entire matter is in a fully ionized state. Inert gases like Argon can serve as an ideal plasma generating agent. A vacuum chamber is pre-pumped down to around 1 milli Torr and the electrode circuit is fired up to a pre-sputtering power level. The inert gas is then introduced to ignite the plasma.

Ever present "free electrons" will immediately be accelerated away from the negatively charged electrode (cathode). These accelerated electrons will approach the outer shell electrons of neutral Ar atoms in their path and, being of a like charge, will drive these electrons off the Ar atoms. This leaves the Ar atom electrically unbalanced since it will have more positively charged protons than negatively charged electrons - thus it is no longer a neutral Ar atom but a positively charged "ion". In this case Ar^+ .

At this point the positively charged Ar^+ ions are accelerated into the negatively charged electrode (cathode) striking the surface and 'blasting' loose electrode material (diode sputtering) and more free electrons by energy transfer. The additional free electrons feed the formation of ions and the continuation of the plasma. During this process free electrons find their way back into the outer

electron shells of the Ar^+ ions thereby changing them back into neutral Ar gas atoms. Due to the laws of conservation of energy, when these electrons return to a ground state, the resultant neutral Ar gas atom has gained energy and must release that same energy in the form of a photon. The release of these photons is the reason the plasma appears to be glowing.

This basic sputtering concept is also known as Diode sputtering. The concept has proven to be a useful technique in the deposition of thin films when the cathode is covered with source material (sputtering target). Diode sputtering however has two major problems:

1. the deposition rate have is slow and
2. the electron bombardment of the substrate is extensive and can cause overheating and structural damage.

There needs to be a way to control the free electrons and limit its bombardment on the substrate. Power levels must be brought down for prolonged processes and the overheating issues needs to be dealt with for longer depositions. This is where Magnetron sputtering addresses these issues.

3.3 Magnetron Sputtering

In the late 1930s Frankfurt Penning developed the ‘electron trap’ to confine electrons near a surface using a combination of electric and magnetic fields. This combination of electric and magnetic fields increased the ionization of the plasma near the surface and was named a “Penning Discharge” after its inventor. Penning used his invention to sputter from the inside of a cylinder. This was an important development in the history of sputtering and formed the first step towards the magnetron sputtering methodology. Such a combination of electric and magnetic fields allowed sputtering to be performed at lower pressures, lower voltages and at higher

deposition rates than were previously possible with DC sputtering without magnets. Variations of the Penning magnetron have subsequently been developed, notably the post cathode magnetron invented by Penfold and Thornton in the 1970s and Mattox, Cuthrell, Peeples and Dreike in the late 1980s.^[27]

Unlike diode sputtering discussed earlier, by using magnets behind the cathode to trap the free electrons in a magnetic field directly above the target surface, these electrons are not free to bombard the substrate to the same extent as with diode sputtering. At the same time the extensive, circuitous path carved by these same electrons when trapped in the magnetic field, enhances their probability of ionizing a neutral gas molecule by several orders of magnitude. This increase in available ions significantly increases the rate at which target material is dislodged and subsequently deposited onto the substrate.

3.4 RF Magnetron Sputtering

In the 1960s the use of radio frequency, RF to sputter material was investigated. Davidse and Maiseel used RF sputtering to produce dielectric films from a dielectric target in 1966. In 1968 Hohenstein co-sputtered glass using RF and metals (Al, Cu, Ni) with DC, to form cermet resistor films. Though this method proved very powerful RF magnetron sputter deposition is not used extensively for commercial PVD for several reasons. The major reasons are it is not economic to use large RF power supplies due to their high cost and the fact that you introduce high temperatures, due to the high self-bias voltage associated with RF power, into insulating materials.^[27] Reflectance power control and superior tuning requirements have left the RF magnetron sputtering the domain of costly R&D centers with the means and technical support for maintenance. Figure 6 shows the working principle of R.F Magnetron sputtering.

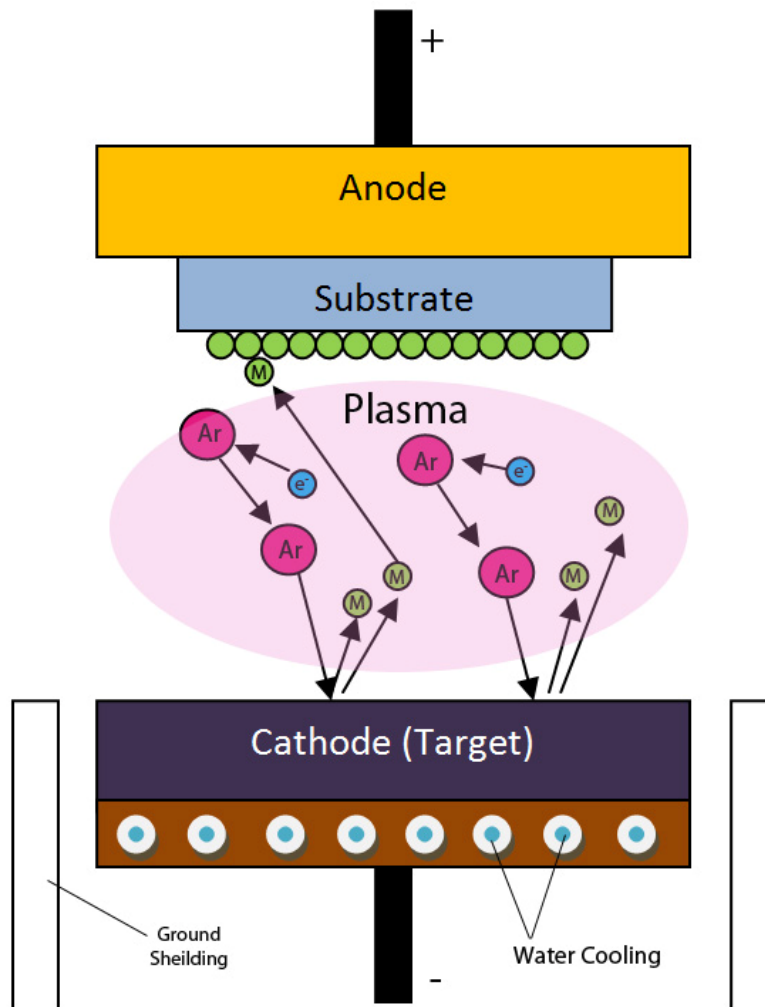


Figure 6. The working of R.F Magnetron Sputtering system. Ar is Argon, M are the metal atoms dislodged from the target, e- are the electrons.

CHAPTER 4: EXPERIMENTAL

4.1 Preparation

The first step is to ensure the target is not broken and that its integrity is assured. The inspected target is then placed on the desired sputtering gun and holstered with the shield and ring holders. It is crucial to make sure there are no contacts with the surface of the target and the sides of the gun. This will lead to a short and blow out the tuner box or other sensitive RF equipment.

The samples need to be prepared carefully for the procedure to keep contaminants to the bare minimum possible. Substrates such as quartz, silicon, cut glass slides are cleaned thoroughly with the correct chemical procedures suited for each type of substrate material. Glass and quartz samples are first immersed in semiconductor grade methanol and are given a 5 minute bath in the sonic-bath apparatus. The sonic-bath apparatus generates gentle but persistent shocks that aid the methanol or other cleaning agents to get the extra force in degreasing the surface of the samples. The samples are then taken out and flushed with inert nitrogen gas to aid quick drying. The samples are then immersed in semiconductor grade Acetone to remove tough organic/oil contaminants and are given another 5 minutes in the sonic-bath. The samples are then taken out and dried under the flush of nitrogen along with quick dips into methanol before being flushed again with nitrogen as fast drying acetone tends to leave irregular stains on the samples.

Silicon wafer samples on the other hand are first immersed in semiconductor grade acetone for 2-3 minutes without a sonic-bath. The samples are rinsed with de-ionized water. The silicon wafers are then immersed in Buffer Oxide Etchant (BOE) for 3 minutes. Safety is paramount

whilst handling dangerous chemicals like the BOE. Full body cover, face guard and gloves are used while handling BOE and the samples. Once the sample is taken out of the BOE it is given a thorough rinse with de-ionized water. Finally to aid drying the sample is flushed with nitrogen.

The samples are carefully placed on clean kim-wipes or lab grade disposable thin tissues while the substrate masks are wiped down with methanol. The samples are then placed on the substrate masks accordingly and lined up ready to be placed on the sputtering chamber's substrate holders.

It is also a good practice in the lab to check the coolant water levels and the compressed gas supply pressures for the pneumatic valve's operations before engaging the sputtering system.

4.2 Equipment

The substrates are placed in their respective sample holders and the chamber lid is properly guided down and shut. The vacuum chamber is connected to a high vacuum cryogenic pump via a main exposure valve. The main chamber is also connected to a mechanical pump that has its own valve to enable exposure to the chamber. The mechanical pump is used to initiate a rough vacuum which will bring the pressure in the main chamber down to about 200 mTorr.

The mechanical pump is switched on followed by the opening of its valve called the 'chamber rough'. The chamber is steadily pumped down towards the 200 milli torr mark. The indicator at first shows the chamber is at atmosphere, this will switch over to the 'xover' indicator that lets the user know it is the right time to close the chamber rough and switch off the mechanical pump. It is imperative to not switch off the mechanical pump before closing the chamber rough,

as failing to do so will force the oil in the pump to flood the chamber. Once the pressure of 200 mTorr is reached the chamber rough is closed and the mechanical pump is switched off.

The high vacuum cryogenic pump is now ready to be exposed to the chamber. Gas molecules wander about because they have energy and this is due to heat. If the heat is brought down their motion can be hampered and slowed to a halt. The cryogenic pump has a cold head that runs at around 8 Kelvin at all times. Such a cold head when exposed to a 200 mTorr vacuum chamber, it is able to suck out the remaining unwanted gas molecules by attracting them to the cold head. Once the main high-vac valve is opened to expose the high vacuum pump, it takes about 2-2.5 hours to reach the desired pressure of 1 mTorr.

4.3 Deposition procedure

Once the pressure of 1 mTorr is achieved the deposition can begin. The shutter to the sample holder cradle right above the operated gun, is covered and the sample holder number is cataloged. The individual gas valves are turned on and ready to be let into the main gas mixing chamber. Initially only Argon is switched on and the flow to the chamber will be set via the mass flow regulators assigned to each gas line. The main gas valve is still closed so there is no introduction of any gases until the flow rates are set. The conductance control is engaged where by the high-vac valve is partially closed to ensure uniform chamber pressure and absorption of spent gasses. Once set, the tuner box and RF power supplies are switched on and the two tuner shunts are engaged for 2 seconds each. The RF power to the gun is then switch on and a nominal power of 25 watts is applied to the gun whilst keeping close watch for any reflectance power spikes. Now the main gas valve is opened and the plasma is seen ignited with a pink glow typical of argon in the absence of other gases. The target is pre-sputtered for 10 minutes with the

shutters to the samples closed to eliminate any surface contaminants on the target. The power during pre-sputtering can be now raised to about 35-40 watts. Once pre-sputtering is over the other gasses are introduced if any and the shutters can be opened and the timers can be set for the deposition to begin.

The shutters are re-engaged once the time period is over before the shutdown procedure is followed. If there next sample is being deposited the substrate holder rotator is engaged to set the next substrate sample up for deposition.

4.4 Shutdown

Once the depositions are over the shutters are re-engaged and power to the gun is slowly reduced to avoid any sudden spikes in reflectance power, it is also a good practice to ensure prolonged life of the gun. Once fully powered down the RF gun supply is switched off and so are the power supplies to the RF unit and tuner box. The main gas valve is close and the process gasses are turned off. The conductance control is released to open the chamber to the high-vacuum and the main high-vacuum valve is re-engaged to completely close off the high vacuum pump from the chamber. Once the chamber is fully isolated the chamber needs to be vented slowly. The nitrogen line is opened and put on standby. The vent option is engaged and the nitrogen flow rate is slowly increased to the point it can be heard rushing steadily into the chamber.

Once at atmospheric pressure the 'xover' status light shuts off and switches over to atmosphere indicator. The chamber is now ready to be opened and the substrate samples can be claimed. All samples must be placed in a sample box cleaned with methanol and padded with kim-wipes to protect the samples.

4.5 Characterization

The grown Y_2O_3 films were characterized by performing structural and optical measurements. X-ray diffraction (XRD) measurements on Y_2O_3 films were by performed using a Bruker D8 Advance x-ray diffractometer. All the measurements were made ex-situ as a function of growth temperature. XRD patterns were recorded using $\text{Cu K}\alpha$ radiation ($\lambda=1.54056 \text{ \AA}$) at RT. The coherently diffracting domain size (D_{hkl}) was calculated from the integral width of the diffraction lines using the Scherrer's equation after background subtraction and correction for instrumental broadening. The Scherrer equation is represented as ^[29]:

$$D_{hkl} = \frac{0.9\lambda}{\beta \cos \theta} \quad \{1\}$$

where D_{hkl} is the size, λ is the wavelength for the anode material used in the XRD machine, β is the width of a peak at half of its intensity, and θ is the angle of the peak.

The surface crystallography of Y_2O_3 was investigated using reflection high-energy electron diffraction (RHEED) measurements. The electron diffraction imaging was performed using 50 keV electron beam in EF-Z4-5 set up.

Ion beam analysis of the Y_2O_3 -Si samples was performed using the 6 MV tandem accelerator. Rutherford backscattering spectra (RBS) were recorded using a 2.0 MeV beam of He^{++} ions with a 0° angle of incidence measured from the sample normal. Backscattered ions were collected using a silicon surface barrier detector at a scattering angle of 165° . Composition profiles were determined by comparing SIMNRA computer simulations of the spectra with the experimental data ^[30].

Optical properties and growth behavior of the grown Y_2O_3 films have been primarily probed by spectroscopic ellipsometry (SE), which measures the relative changes in the amplitude and phase of the linearly polarized monochromatic incident light upon oblique reflection from the sample surface. The experimental parameters obtained by SE are the angles Ψ (azimuth) and Δ (phase change), which are related to the microstructure and optical properties, defined by ^[31-34]

$$\rho = R_p/R_s = \tan \Psi \exp (i\Delta) \quad \{2\}$$

where R_p and R_s are the complex reflection coefficients of the light polarized parallel and perpendicular to the plane of incidence, respectively. Ellipsometric parameters Ψ and Δ were measured over wavelength range 250-900 nm employing SPECTROSCAN ellipsometer. The device spectral resolution is 2 nm and the input angle of light beam is 70° in reference to surface normal. Four-zone method of measurements was used with averaging over all four zones. To calculate the optical constants, namely the index of refraction (n) and extinction coefficient (k), and their wavelength dispersion profiles for Y_2O_3 films the following optical model was used: isotropic substrate – isotropic homogeneous film – air.

CHAPTER 5: RESULTS AND DISCUSSION

5.1 Structure and growth behavior

The XRD patterns of Y_2O_3 films are shown in Figure 7. The XRD curves of Y_2O_3 films grown at RT-100 °C did not show any peaks indicating their characteristic amorphous ($\alpha\text{-Y}_2\text{O}_3$) nature. The XRD peak (JCPDS 43-613) corresponding to cubic phase ($\text{c-Y}_2\text{O}_3$) began to appear for Y_2O_3 samples grown at $T_s=200$ °C.

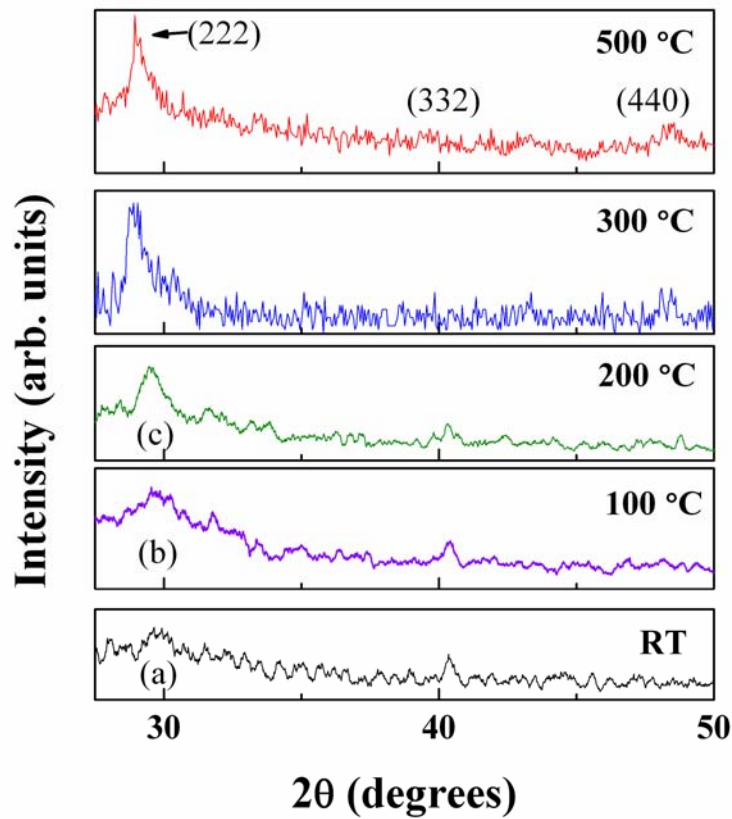


Figure 7. XRD patterns of Y_2O_3 films grown on Si(100) substrates. The structural changes with increasing growth temperature are evident. Room temperature grown Y_2O_3 films are amorphous while those at higher temperatures are nanocrystalline. The randomly oriented

However, the peak (at $\sim 28^\circ$) is rather broad indicating the presence of small nanoparticles. It is evident (Figure 7) that the intensity of the peak, which corresponds to diffraction from (222) planes, increases with increasing T_s . This is an indicative of an increase in the average grain-size with increasing T_s . The crystallite size D_{hkl} calculated using the Scherrer equation is found to be in the range of 15-40 nm for Y_2O_3 films grown in the range of $T_s=200-500^\circ C$. The (440) peak began to appear at $T_s \geq 300^\circ C$. The appearance of specific diffraction peaks indicate that the growth process initiates with (111) planes due to the lowest surface energy ^[24]. With increasing temperature, the in-plane organization of the structure and random oriented nanograins results in the other characteristic peaks. Most important to note is the diffuse nature of XRD curves, in spite of the appearance of (222) peak, indicating the nano-crystallites embedded in the amorphous matrix.

The RHEED patterns of Y_2O_3 films grown at different temperatures are shown in Figure 8. RHEED patterns also confirm that the Y_2O_3 films grown at RT-100 $^\circ C$ (Figure 8a) were completely amorphous. The onset of ring patterns indicating the crystalline nature of the Y_2O_3 films began at 200 $^\circ C$. A further increase in T_s indicates the formation of well defined polycrystalline nature of the Y_2O_3 films. The observed electron diffraction patterns match with the cubic- Y_2O_3 (JCPDS 43-613). The XRD and RHEED results are in good agreement and confirm the improved structural quality of the Y_2O_3 films with increasing growth temperature.

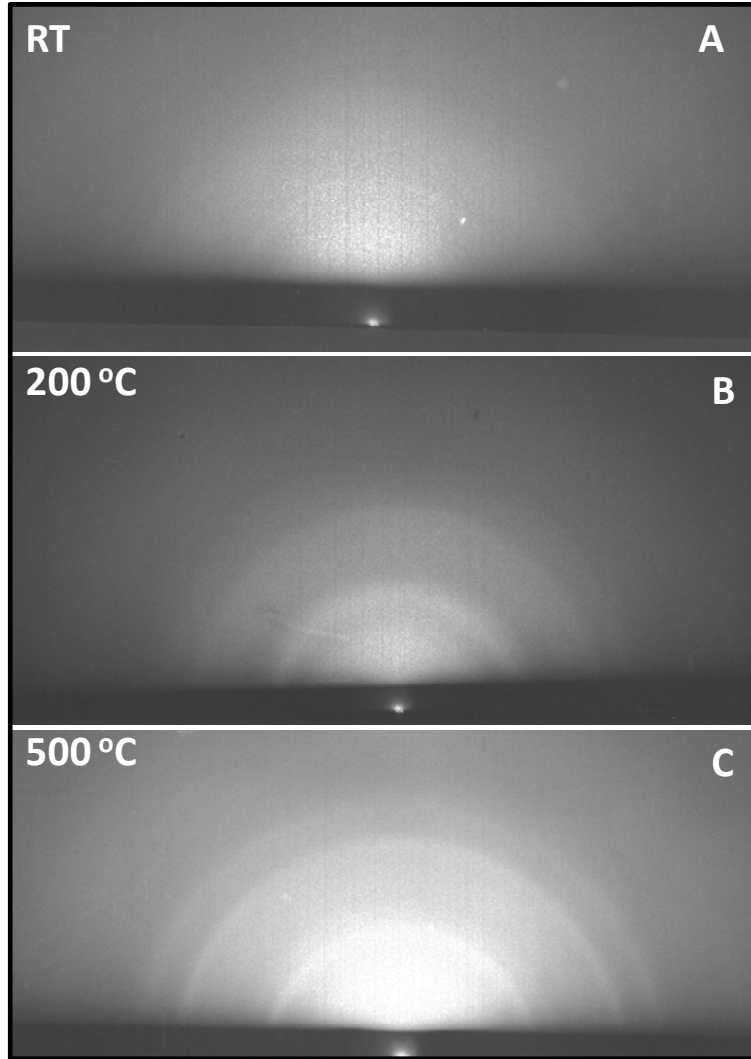


Figure 8. RHEED patterns of Y_2O_3 films. The broad and diffuse background of the RHEED pattern obtained for Y_2O_3 films grown at room temperature (image A) indicate the amorphous nature. Onset of crystallization of the Y_2O_3 films can be noted with increasing T_s to 200 °C (image B). The RHEED pattern (image C) for samples grown at 500 °C indicates the well-defined, cubic structured Y_2O_3 films.

In order to obtain information on the growth behavior and kinetics involved, the average grain size (determined from XRD) variation as a function T_s is examined. The average grain size (L) variation with T_s is shown in Figure 9.

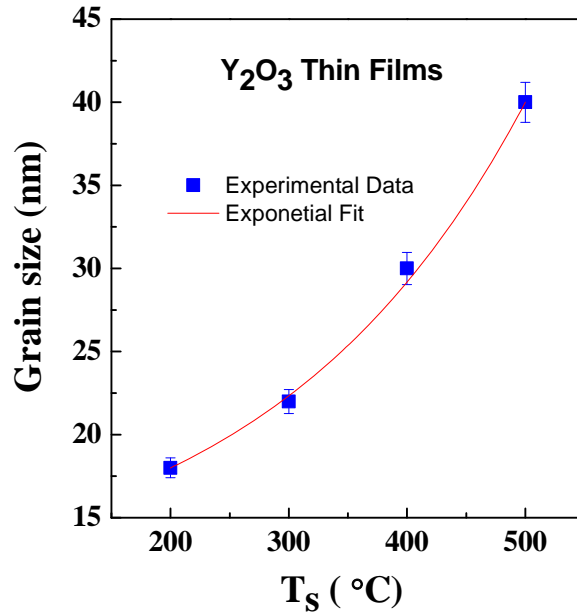


Figure 9. Variation of grain size of Y_2O_3 films with growth temperature. The experimental data along with the fit to the exponential function according to eq. 3 are shown. Excellent agreement between the observed data and fit suggests the thermally activated growth process of sputter-deposited Y_2O_3 films.

It must be emphasized that the grain size indicated at $T_s < 200\text{ }^{\circ}\text{C}$ is based on the fact that the SEM images have occasionally shown the grains of $\leq 6\text{ nm}$ which are embedded in the amorphous matrix. However, most of the film volume is amorphous and didn't reveal even a sign of localized structural order with other spectroscopic or X-ray diffraction analysis. Based on the observed results, the growth behavior of Y_2O_3 films can be conveniently divided into two zones, where the structural differences are significant. The first category or zone contains the set of Y_2O_3 films grown at temperatures $< 200\text{ }^{\circ}\text{C}$. The second is the set of Y_2O_3 films grown at temperatures $\geq 200\text{ }^{\circ}\text{C}$. If temperature is low such that the period of the atomic jump process of adatoms on the substrate surface is very large, the condensed species may stay stuck to the regions where they are landing thus leading to an amorphous Y_2O_3 films. The adatom mobility

on the surface increases with increasing T_s [35,36]. The XRD and RHEED analyses clearly indicate that 300 °C is the critical temperature to promote the growth of nanocrystalline Y_2O_3 films. For the given set of experimental conditions, a temperature of 200 °C is, therefore, favorable to provide sufficient energy for Y_2O_3 crystallization. A functional relationship obtained between the average particle size (L) and the temperature fits to an exponential growth function (Figure 9). The data supports thermally activated growth process of nanocrystalline Y_2O_3 films. Therefore, similar to the diffusion coefficient equation [36,37] L can be expressed as:

$$L = L_0 \exp (-\Delta E/k_B T) \quad \{3\}$$

where L is the average grain size, L_0 is a pre-exponential factor or proportionality constant which depends on the specific film, substrate materials involved, ΔE the activation energy, k_B the Boltzmann constant and T (T_s+273 K) the absolute temperature. It is important to recognize the data fits well to the functional relationship indicating thermally driven growth of nanocrystalline Y_2O_3 films. The activation energy derived from fitting is ~0.12 eV.

5.2 Chemical Composition

The Rutherford backscattering (RBS) spectra Y_2O_3 films are shown in Figure 10. The backscattered ions observed were due to various elements, and the positions are indicated by arrows for the experimental spectrum. The scattering from yttrium, the heaviest among the elements present either in the film or substrate, occurs at higher backscattered energy as shown in RBS curves for Y_2O_3 films (Figure 10).

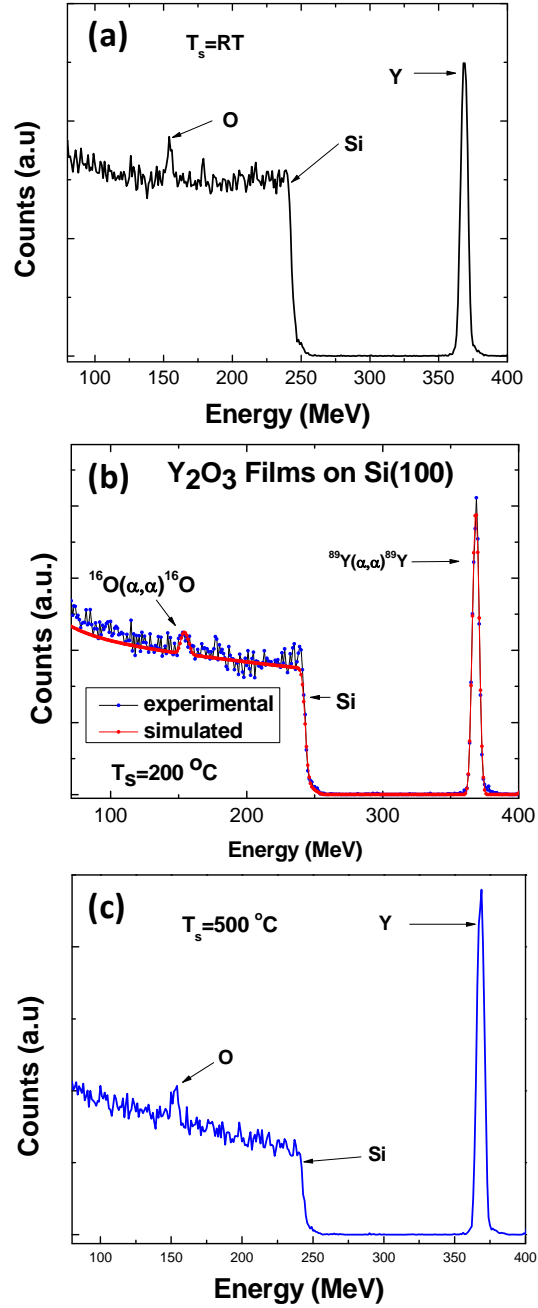


Figure 10. RBS spectra of Y_2O_3 films grown at various temperatures. The scattering due to O and Y in the grown films and Si from substrate are as indicated. The spectra shown are: (a) $T_s = RT$, (b) $T_s = 200\text{ }^\circ\text{C}$, and (c) $T_s = 500\text{ }^\circ\text{C}$. The SIMNRA fitting method utilized in determining the stoichiometry of the samples is outlined for the case of $T_s = 200\text{ }^\circ\text{C}$. The experimental (circles) and simulated (line) RBS curves are shown. Excellent agreement between the experimental and calculated curves can be noted.

The measured height and width of this peak is related to the concentration and thickness distribution of yttrium in the oxide film and serves as a calibration check for composition and thickness since known Rutherford scattering cross section and experimental parameters can be used to calculate this height and width ^[35]. The procedure utilized to derive the chemical composition of the grown films is represented for the samples grown at 200 °C (Figure 10b). The experimental curve (circles) along with the simulation curve (lines) calculated using SIMNRA code is as shown in Figure 10b. The simulated curve was calculated using SIMNRA code ^[30] for the fixed set of experimental parameters:

- (1) incident He^+ ion energy,
- (2) integrated charge,
- (3) energy resolution of the detector, and
- (4) scattering geometry.

It can be seen in Fig. 4b that the simulated curve (solid line) calculated using the experimental parameters is in good agreement with the experimental RBS spectrum. This observation indicates that film had a stoichiometric Y_2O_3 composition. The O/Y ratio determined from RBS analysis using the absolute concentration of O and Y from the experimental curve for films grown at 200 °C is 1.49, which is an excellent agreement with that (1.5) of the stoichiometric Y_2O_3 . RBS analysis as a function of T_s revealed that the chemical composition is well maintained in the films grown at $T_s=200$ °C. The O/Y ratio variation of the Y_2O_3 films as a function of growth temperature is shown in Figure 11. RBS analysis indicates an excess O/Y ratio of 2.1 for Y_2O_3 films grown at RT (Figure 11).

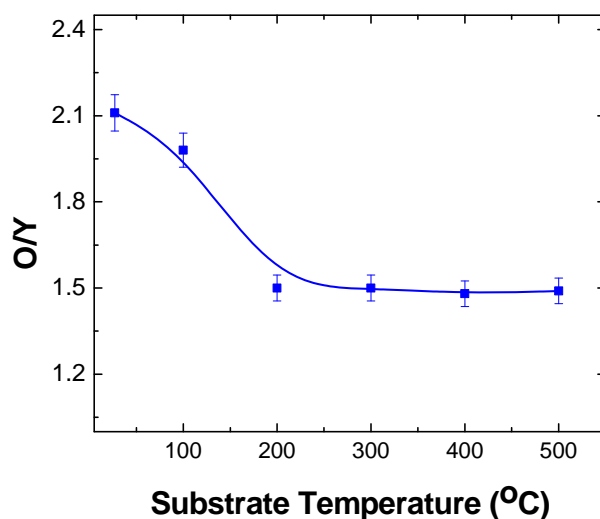


Figure 11. The atomic ratio of oxygen to yttrium in Y₂O₃ films grown at various temperatures. It is evident that the films grown at lower temperatures are nonstoichiometric while the stoichiometric Y₂O₃ film formation occurs in the temperature range of 200-500 °C.

The concentration of O was found much higher than Y concentration. Perhaps, the temperature is not enough to promote the reactive process in order for Y to fully oxidize to form Y₂O₃ phase. This result indicates that a temperature of 200 °C or higher is required for the formation of stoichiometric Y₂O₃ films. The O/Y ratio deviating from expected the stoichiometry and formation of excess oxygen with a metal deficiency was also reported for ion-beam sputter-deposited Y₂O₃ films on Si. The reported value for room temperature grown ion-beam sputter-deposited Y₂O₃ films on Si was 2.57, which is much higher than the present work. It seems that the deviation from stoichiometric due to incomplete oxidation of Y at room temperature is, at least, common for film growth by physical vapor deposition processes.

5.3 Optical Constants

The spectral dependencies of the ellipsometric parameters, Ψ and Δ , determined for Y_2O_3 samples are shown in Figure 12. The spectral dependencies of Ψ and Δ can be fitted with appropriate models to extract film thickness and the optical constants based on the best fit between experimental and simulated spectra ^[32,33]. The curves obtained for Y_2O_3 films indicate (Figure 12) a reasonable agreement between the experimental and simulation data. Adjusting the spectral dependencies of ellipsometric parameters over complete spectral range for m wavelength points was achieved with minimization of error function, which is defined as ^[31-34]

$$\sigma^2 = \frac{1}{m} \cdot \sum_{i=1}^m \left[\left(\Delta_{\text{exp.}} - \Delta_{\text{calc.}} \right)^2 + \left(\Psi_{\text{exp.}} - \Psi_{\text{calc.}} \right)^2 \right] \quad \{4\}$$

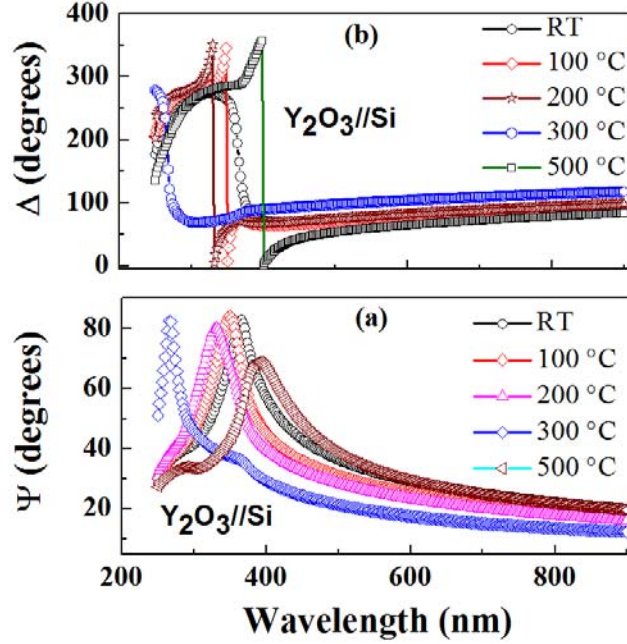


Figure 12. The spectral dependence of Ψ and Δ for Y_2O_3 films. A significant shift of Ψ and Δ with a change in nanostructure and grain size of Y_2O_3 films is evident from the curves.

The notable characteristic feature observed is the evolution of the ellipsometric functions, $\Psi(\lambda)$ and $\Delta(\lambda)$. The behavior is remarkably different for Y_2O_3 samples as a function of structural transformation from a- Y_2O_3 to nc- Y_2O_3 and the average grain-size. These observations indicate that the microstructure strongly influence the optical properties of Y_2O_3 thin films.

The spectral dependence of the extinction coefficient determined from SE data for Y_2O_3 films is shown in Figure 13. It is evident that the extinction coefficient values are low and very close to zero in most part of the spectral region (Figure 13).

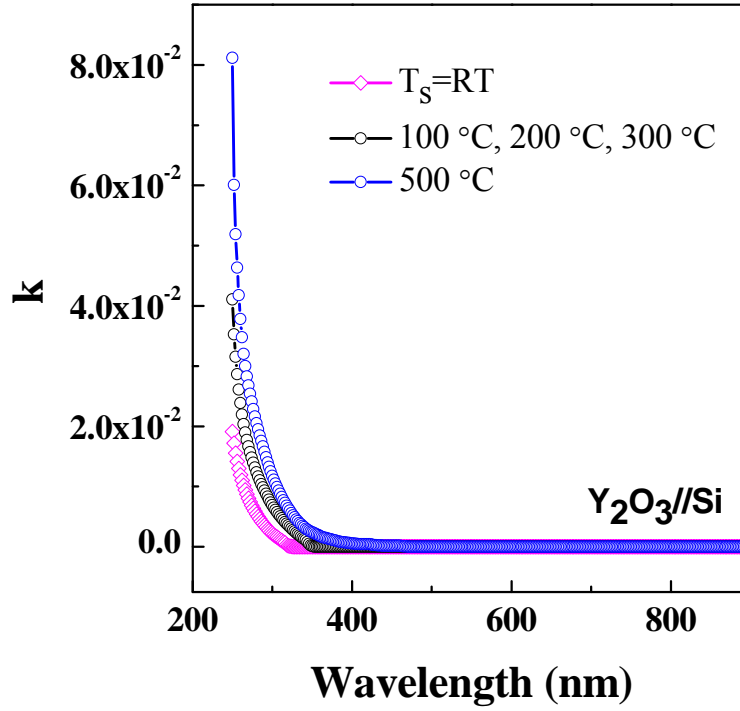


Figure 13. The spectral dependence of k for Y_2O_3 films as a T_s . The spectra reveal that the k values are almost zero in the visible and near infrared regions. The sharp increase in the k values near shorter wavelengths are due to fundamental absorption across the band gap of the Y_2O_3 films.

It is important to recognize this feature, which indicates very low optical losses due to absorption. The onset or sharp increase in k at short wavelengths is due to the fundamental absorption across the band gap. The dispersion function $k(\lambda)$ (for short-wavelength part of spectrum) was approximated by Cauchy's polynomial ^[38,39]:

$$k(\lambda) = a + \frac{b}{\lambda^2} + \frac{c}{\lambda^4} \quad \{5\}$$

where a, b , and c are constants, which are specific to the material. It can be seen that the data fits well to the calculations as shown in Figure 13.

An understanding of the structural quality of Y_2O_3 films can also be derived from the dispersion profiles of $k(\lambda)$. Specifically, the $k(\lambda)$ spectral curves (Figure 13) indicate that the k value of the Y_2O_3 films is almost zero in the visible and near infrared spectral regions, while for photon energies above ~ 5 eV, the extinction coefficient increases sharply. This effect is specifically more pronounced for Y_2O_3 films grown at 500°C , while some tailing can be noted for Y_2O_3 films grown at RT. The extinction differences in these films are obviously related to the structural quality difference in the films. The relatively weak absorption and tailing behavior observed for the Y_2O_3 films grown at RT can be attributed to a high density of defect states in the band gap. The defect states may be arising from the amorphous nature of the films where the structural disorder is high compared to those Y_2O_3 films grown at higher temperatures. The progressive structural improvement in the Y_2O_3 films as a function of increased growth temperature decreases the defect density and, hence, a sharp increase in optical absorption. The situation is totally different in Y_2O_3 films grown at $T_s=500^\circ\text{C}$. The k value increases sharply at shorter wavelengths. Such behavior is expected for a film with sharp band edge profiles without defect states into the band gap. Therefore, the Y_2O_3 films with well ordered, cubic nano-grains exhibit a sharper optical absorption and k values compared to Y_2O_3 films grown at lower temperatures. Most importantly, the observed variations in the dispersion profiles of $k(\lambda)$ are in corroboration with the XRD and RHEED results where the structural quality differences of Y_2O_3 films are evident. Furthermore, evidence for stoichiometric defects of Y_2O_3 films grown at temperatures less than 200°C comes from the RBS analysis (Figure 10).

The dispersion profiles of ' n ' determined from SE data for Y_2O_3 films are shown in Figure 14. The results indicate a similar behavior as noted in $k(\lambda)$ curves. The ' n ' dispersion curves also

indicate a sharp increase at shorter wavelengths corresponding to fundamental absorption of energy across the band gap.

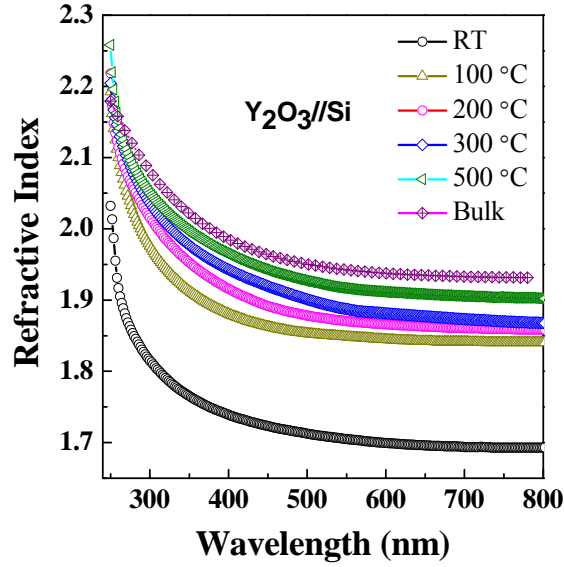


Figure 14. The spectral dependence of the index of refraction (n) of Y_2O_3 films as a function of growth conditions. A marked difference in the n profiles is evident for nanocrystalline Y_2O_3 when compared to the amorphous Y_2O_3 . The curves demonstrate that the n values are dependent on the grain size. Enhancement in n values for nanocrystalline Y_2O_3 is due to increased grain size. The profile of bulk Y_2O_3 is shown for comparison. It is evident that the randomly oriented, cubic- Y_2O_3 nanocrystallites grown at 500 °C exhibit the best profile that is comparable to that of bulk.

The ‘structure and grain-size’ dependence is evident in the dispersion curves (Figure 14), where there is an increase in ‘ n ’ values when there is a transformation from a- Y_2O_3 to nc- Y_2O_3 . In addition, difference in the curves for nc- Y_2O_3 arise due increase in the average grain-size. Most important to mention is that the refractive index dispersion for Y_2O_3 films is comparable to that of bulk ^[40] (single crystal) Y_2O_3 (Fig. 8). The dispersion function $n(\lambda)$ (for short-wavelength part of spectrum) for Y_2O_3 films was also approximated by Cauchy’s polynomials ^[38,39]:

$$n(\lambda) = d + \frac{e}{\lambda^2} + \frac{f}{\lambda^4} \quad \{6\}$$

where d , e and f are constants, which are specific to the material. It can be seen that the data fits well to the calculations as shown in Figure 14.

A simple model can be formulated to explain the observed functional relationship between the optical constants and nanostructure in nc- Y_2O_3 films. Evident from the results, the dispersion of optical constants depend on the structural quality, chemistry and grain size. XRD and RHEED measurements evidenced that Y_2O_3 films grown at RT are completely amorphous. RBS indicates the stoichiometric defects. It is, therefore, reasonable to attribute the observed low values of n and k to a very low packing density in the Y_2O_3 films. These films, which are characterized by a structural disorder, may be porous causing a decrease in optical constants. The initial increase in n and k values when Y_2O_3 films are grown at intermediate temperatures (200 °C) is due to a structural transformation from a- Y_2O_3 to nc- Y_2O_3 as noted in XRD and RHEED measurements. Therefore, we believe that the packing density slightly improves but not significantly. Perhaps, there may be amorphous background as indicated by RHEED patterns. Furthermore, the XRD patterns are rather broad and diffuse indicating amorphous nature and lack of long-range order, existence of localized grain but embedded in an amorphous network leading to the observed increase n and k values for samples grown at intermediate temperatures. Such behavior was also noticed in ZnO ^[41] and CeO_2 ^[42]. The situation is remarkably different for Y_2O_3 samples grown at the highest temperature, 500 °C. The evolution of cubic phase is evident from both XRD and RHEED. RBS analysis indicates the complete oxidation and formation of stoichiometric Y_2O_3 formation. Improved structural order results in the formation of a dense network of nanocrystals leading to an enhancement in the packing density. This characteristic change in structure results in the observed enhancement in “ n .” It has been argued by several research groups ^[31,34,42,44] that the factors that affect the optical constants are: secondary phase formation, changes in film

stoichiometry, microstructure changes and packing density. Furthermore, most of the earlier works were performed either on the as-grown or annealed Y_2O_3 films, where the possibility is for either an amorphous or a preferred/textured polycrystalline structure. However, in nc- Y_2O_3 films, the nanostructure is characterized by dense, randomly oriented nanocrystals. This leads to enhancement in packing density, which results in enhanced density of absorption and index of refraction. The additional evidence for the proposed mechanism comes from our earlier reports on the optical properties of nanocrystalline WO_3 [43] films and other reports existing in the literature [42,43].

5.4 Electrical Characteristics

The room temperature AC electrical conductivity variation (at 20 Hz) of Y_2O_3 films with T_s is shown in Figure 15.

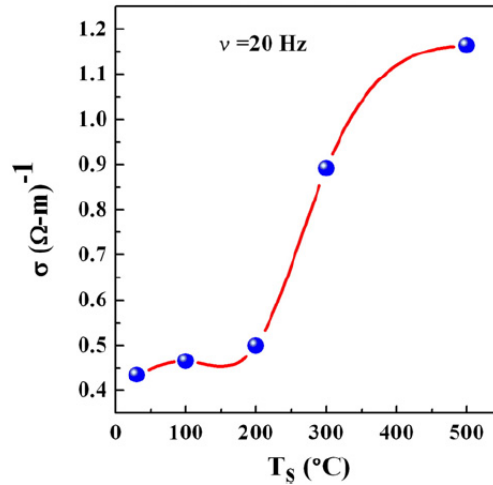


Figure 15. Variation of the electrical conductivity of Y_2O_3 with T_s . The conductivity increase with increasing grain size is evident from the curve.

It can be seen that the electrical conductivity increases from $0.4 (\Omega\text{-m})^{-1}$ to $1.2 (\Omega\text{-m})^{-1}$ with increasing T_s . The conductivity is reported to decrease with grain-size reduction due to the increasing grain-boundary volume and associated impedance to the flow of charge carriers ^[45,46]. If the size is smaller than the electron mean free path, grain-boundary scattering dominates and, hence, the electrical conductivity decreases. The electrical conductivity is also very sensitive to lattice imperfections in solids, such as vacancies and dislocations which are reported to be present in nanocrystalline materials ^[45,46]. In addition, lattice strain and the distortions can affect the motion of charge causing decrease in conductivity ^[47,48]. The room-temperature conductivity data and its variation with T_s observed for Y_2O_3 can be explained taking these factors into consideration. Y_2O_3 films grown at RT-100 °C are amorphous as evidenced in XRD studies. The randomness or disordered structure of the films, therefore, accounts for the high resistivity of Y_2O_3 films. XRD peak evolution and an increase in the average grain-size indicate that the structural order improves with increasing T_s . Therefore, decrease in resistivity with increasing T_s can be attributed to the improved structural order and grain-size.

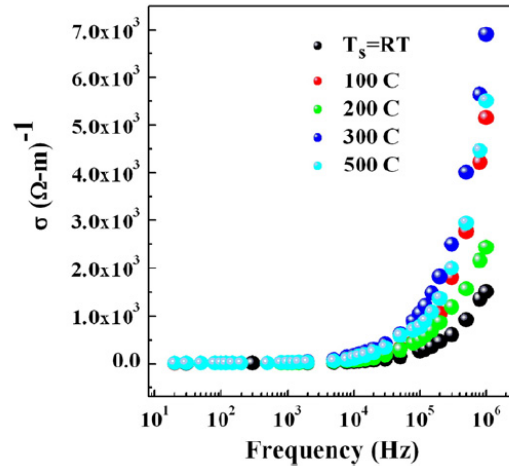


Figure 16. Frequency dependent conductivity of Y_2O_3 . The dispersion relation is shown with increasing T_s .

The frequency dependence of the electrical conductivity (σ_{ac}) of Y_2O_3 films is shown in Figure 16. The total conductivity of the films can be expressed by the relationship ^[49]:

$$\sigma_{tot} = \sigma_0(T) + \sigma(\omega, T) \quad \{7\}$$

The first term ($\sigma_0(T)$) of Eq. (7) represents the dc conductivity due to the band conduction, which is frequency independent. On the other hand, the second term of the equation ($\sigma(\omega, T)$) represents the frequency dependent part i.e., the ac conductivity due to the electron hopping between the Y^{3+} ions. The hopping mechanism in Y_2O_3 films is attributed to the presence of oxygen vacancies ^[50]. Based on the Y_2O_3 bulk electronic structure, the valence band is formed by the filled O 2p orbital and the conduction band is formed by the metal (Y) 5d orbital. The vacancy level forms below the conduction band and it can also trap one or two electrons. A trapped electron causes the adjacent Y ions to distort asymmetrically, pulling down a singly degenerate B1 state from the conduction band. This state can be occupied by 1 or 2 electrons. Conductivity increase (by three orders of magnitude) with increasing frequency from 20 Hz to 1 MHz is attributed due to the hopping mechanism in Y_2O_3 films. While $\sigma_{ac} \sim 10^{-3} \Omega^{-1}\text{-cm}^{-1}$ at low frequencies (20 Hz), σ_{ac} increases to $\sim 101 \Omega^{-1}\text{-cm}^{-1}$ at higher frequencies (1 MHz).

The observed dispersion in the resistivity is due to the contribution from the Y and O ions to the relaxation. At low frequency regime, hopping of electrons between the localized Y ions increases subsequently the resistivity decreases. At high frequencies, the hopping of electrons could not follow the applied field and hence becomes almost constant (Fig. 10). The frequency variation of electrical resistivity data was fit to the following equation ^[51]

$$\rho - \rho_{\infty} = \frac{\rho_0 - \rho_{\infty}}{1 + (\omega\tau)^{2(1-\alpha)}} \quad \{8\}$$

where ρ_{∞} is the resistivity value at 1 MHz, ρ_0 is the resistivity value at 20 Hz, τ is the mean relaxation time and α is the spreading factor about the mean relaxation time. The τ values determined from fitting of the data lie in the range of 2.8–1.4 μs for Y_2O_3 films grown at $T_s = \text{RT} - 500$ C. On the other hand, α value varied in the range of 0.41–0.35.

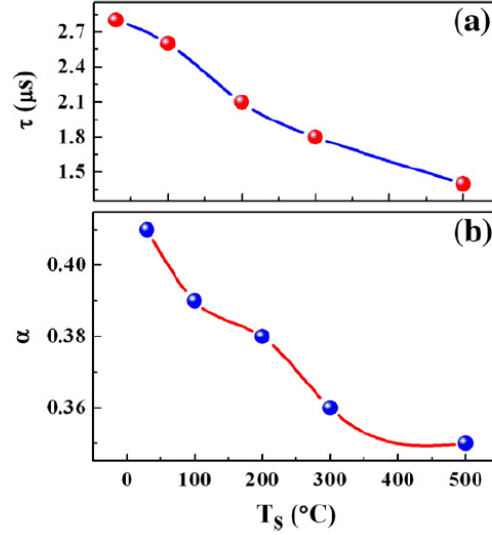


Figure 17. (a) Variation of the mean relaxation time (τ); (b) the spreading factor (α) with increasing T_s . τ and α are seen to decrease with increasing T_s .

The functional relationship between τ/α and T_s is shown in Figure 17. The variation of τ and α makes it clear that the effect of T_s and, hence, microstructure is significant on the ac electrical conductivity of Y_2O_3 films. The τ and α values decrease with increasing T_s . This can be understood as follows. Usually, an increase in the hopping distance either due to perturbation to the structure or doping larger ions causes the mean relaxation time and spreading factor to increase^[52,53]. However, in the present case, no additional factors, such as doping, are involved. So, the changes in τ and α must be originating from a difference in the structural quality of the Y_2O_3 films as a function of T_s . It is evident from XRD studies that the Y_2O_3 films grown at

$T_s = RT - 100$ °C are completely amorphous while the structural order improves as the T_s increases toward 500 °C. Therefore, we can attribute that the hopping in amorphous/disordered Y_2O_3 films leads to increased relaxation time associated with a larger spread factor. Improved structural order associated with an increase in grain-size with increasing T_s , as seen in XRD results, subsequently decreases the grain-boundary scattering leading to the observed decrease of the electrical resistivity and, hence, the mean relaxation time and spread factor ^[54].

CHAPTER 6: CONCLUSIONS

The deposition conditions were optimized to viable growth parameters that can be commercially applied. Nanocrystalline Y_2O_3 films with an average grain-size ≤ 40 nm were grown and the relationship between nanostructure and optical properties is investigated. XRD and RHEED measurements demonstrate that the Y_2O_3 films are fully amorphous for $T_s = \text{RT} - 200^\circ\text{C}$, at which point there is a amorphous-to-crystalline transformation. RBS analysis of Y_2O_3 films indicate that amorphous Y_2O_3 films are also characterized by the presence of stoichiometric defects due to incomplete oxidation. Complete oxidation leading to stoichiometric Y_2O_3 film formation occurs at growth temperatures of $200\text{-}500^\circ\text{C}$. The structure and size-effects were significant on the optical constants and their dispersion profiles. A significant enhancement in the index of refraction is observed in randomly oriented dense, cubic- Y_2O_3 nanocrystalline films. A direct, linear functional relationship between the grain-size and refractive index is established for nanocrystalline- Y_2O_3 films.

Room temperature electrical conductivity increases from $0.4 (\Omega\text{-m})^{-1}$ to $1.2(\Omega\text{-m})^{-1}$ with increasing T_s from RT to 500°C . Improved structural order along with a decrease in grain boundary contribution to the scattering with increasing T_s leads to an increase in ac electrical conductivity. Frequency variation of the electrical resistivity fits to the modified Debye's function. Frequency dependent dispersion of the electrical resistivity is due to the contribution from the Y and O ions to the relaxation. Mean relaxation time and the spread factor are sensitive to T_s and, hence, the microstructure of Y_2O_3 film.

REFERENCES

- [1] James Laudon (Sun Microsystems), Performance/Watt: the new server focus: ACM SIGARCH Computer Architecture News - Special issue, Volume 33 Issue 4, November 2005.
- [2] <http://www.theinquirer.net/inquirer/news/1026758/desktop-chips-hit-15ghz-2010>
- [3] <http://www.anandtech.com/show/876/5>
- [4] N. Novkovski*, E. Atanassova, Approaching the limit of the SiO₂ possibilities for application in nanoscale microelectronics, Journal of optoelectronics and advanced materials Vol. 8, No. 3, June 2006, p. 1238 - 1242
- [5] Robert S. Chau; Intel's breakthrough in high-K gate dielectric drives Moore's law well into the future, Jan 2004 Technology@Intel magazine.
- [6] Ghani, T.; Mistry, K.; Packan, P.; Thompson, S.; Stettler, M.; Tyagi, S.; Bohr, M.; Scaling challenges and device design requirements for high performance sub-50 nm gate length planar CMOS transistors, VLSI Technology, 2000. Digest of Technical Papers. 2000, 0-7803-6305-1
- [7] Intel reinvents the transistor, <http://betanews.com/2007/01/27/intel-reinvents-the-transistor/>
- [8] G. D. Wilk, R. M. Wallace, and J. M. Anthony High- κ gate dielectrics: Current status and materials properties considerations.
- [9] Peter H. Koehn, Underneath Kyoto: Emerging Subnational Government Initiatives and Incipient Issue-Bundling Opportunities in China and the United States.

- [10] Angus I. Kingon*, Jon-Paul Maria* & S. K. Streiffner, Alternative dielectrics to silicon dioxide for memory and logic devices, *Nature* | Vol 406 | 31 August 2000
- [11] Wilk, G. D.; Wallace, R. M.; Anthony, J. M. *J. Appl. Phys.* 2001, 89, 5243.
- [12] Niinistö, J.; Putkonen, M.; Niinistö, L. *Chem. Mater.* 2004, 16, 2953.
- [13] Kwo, J.; Hong, M.; Kortan, A.R.; Queeney, K.T.; Chabal, Y.J.; Mannaerts, J.P.; Boone, T.; Krajewski, J.J.; Sergent, A.M.; Rosamilla, J.M. *Appl. Phys. Lett.* 2000, 77, 130.
- [14] Paumier, F.; Gaboriaud, R.J.; Kaul, A. *Cryst. Engg.* 2002, 5, 169.
- [15] de Rouffignac, P.; Park, J.-S.; Gordon, R.G. *Chem. Mater.* 2005, 17, 4808.
- [16] Gordon, W.O.; Tissue, B.M.; Morris, J.R. *J. Phys. Chem. C* 2007, 111, 3233.
- [17] Zhang, S.; Xiao, R. *J. Appl. Phys.* 1998, 83, 3842.
- [18] Zhao, Y.; Kita, K.; Kyuno, K.; Toriumi, A. *Appl. Phys. Lett.* 2009, 94, 042901.
- [19] Rastogi, A.C.; Sharma, R.N. *Semicond. Sci. Technol.* 2001, 16, 641.
- [20] Cho, J.Y.; Ko, K.-Y.; Do, Y.R. *Thin Solid Films* 2007, 515, 3373.
- [21] Lau, W.M. *Appl. Phys. Lett.* 1989, 54, 338.
- [22] Chiam, S.Y.; Chim, W.K.; Pi, C.; Huan, A.C.H.; Wang, S.J.; Pan, J.S.; Turner, S.; Zhang, J. *J. Appl. Phys.* 2008, 103, 083702.
- [23] Tan, Y.N.; Chim, W.K.; Cho, B.J.; Choi, W.K. *IEEE Trans. Electron Devices* 2004, 51, 1143.
- [24] Gaboriaud, R.J.; Pailloux, F.; Guerin, P.; Paumier, F. *Thin Solid Films* 2001, 400, 106.
- [25] Minami, T.; Yamazaki, M.; Miyata, T.; Kobayashi, Y.; Shirai, T. *Thin Solid Films* 2002, 411, 161.

- [26] Tung-Ming Pan Wen-Wei Yeh, High-Performance High- κ Y_2O_3 SONOS-Type Flash Memory.
- [27] History of PVD - Coatings, <http://www.pvd-coatings.co.uk/history-pvd-coatings/>
- [28] R. Behrisch (ed.) (1981). Sputtering by Particle bombardment:. Springer, Berlin. ISBN 978-3540105213.
- [29] Cullity, B.D.; Stock, S.R. Elements of X-Ray Diffraction, 3rd Ed., Prentice-Hall Inc., 2001
- [30] Mayer, M. SIMNRA User's Guide, Technical Report IPP 9/113, Max- Planck-Institut fur Plasmaphysik, Garching, Germany, 1997
- [31] Ramana, C.V.; Utsunomiya, S.; Ewing, R.C.; Becker, U; Atuchin, V.V.; Aliev, V.Sh.; Kruchinin, V.N. Appl. Phys. Lett. 2008, 92, 011917.
- [32] Jellison, Jr., G.E.; Thin Solid Films 1998, 13, 33.
- [33] Fujiwara, H. Spectroscopic Ellipsometry: Principles and Applications, John Wiley & Sons Inc. 2007.
- [34] Atuchin, V.V.; Kruchinin, V.N.; Kalinkin, A.V.; Aliev V.Sh.; Rykhlitskii, S.V.; Shvets, V.A.; Specivtsev, E.V. Opt. Spectr. 2009, 106, 72.
- [35] Ramana, C.V.; Smith, R.J.; Hussain, O.M.; Chusuei, C.C.; Julien, C.M. Chemistry of Materials 2005, 17, 1213.
- [36] Kalidindi, N.R.; Manciu, F.S.; Ramana, C.V. ACS Appl. Mater. Inter. 2011, 3, 863.
- [37] Kittel, C., Introduction to Solid State Physics, Wiley, New York, 1968.
- [38] Aspnes, D.E. The accurate determination of optical properties by ellipsometry, Handbook of Optical Constants of Solids, Academic Press, 1985, pp. 759–760.
- [39] F. Wooten, Optical Properties of Solids, Academic Press, New York, 1972.

- [40] Nigara, Y.; Jpn. J. Appl. Phys. 1968, 17, 404.
- [41] Malandrino, G.; Blandion, M.; Fragala, M.E.; Losurdo, M.; Bruno, G. J. Phys. Chem. B 2008, 112, 9595.
- [42] Toro, R.G.; Malandrino, G.; Blandion, M.; Fragala, I.L.; Nigro, R.L.; Losurdo, M.; Bruno, G. J. Phys. Chem. B 2004, 108, 16357.
- [43] Gullapalli, S.K.; Vemuri, R.S.; Ramana, C.V. Appl. Phys. Lett. 2010, 96, 171903.
- [44] Gibbons, B.J.; Hawley, M.E.; Trolier-McKinstry, S.; Schlom, D.G. J. Vac. Sci. Technol. A 2001, 19, 584.
- [45] N.R. Kalidindi, K. Kamala Bharathi, C.V. Ramana, Appl. Phys. Lett. 97 (2010) 142107.
- [46] R.S. Vemuri, K. Kamala Bharathi, S.K. Gullapalli, C.V. Ramana, ACS Appl. Mater. Interfaces 2 (2010) 2623.
- [47] C.V. Ramana, R.J. Smith, C.M. Julien, J. Vac. Sci. Technol., A 22 (2004) 2453.
- [48] C.V. Ramana, C.M. Julien, Chem. Phys. Lett. 428 (2006) 114.
- [49] K. Kamala Bharathi, G. Markandeyulu, C.V. Ramana, J. Phys. Chem. C 115 (2011) 514.
- [50] S. Ikeda, K. Ogawa, J. Electron Microsc. 41 (1992) 330.
- [51] J. Smith, H.P.J. Wijn, Ferrites, Philips Technical Library, Eindhoven Holland, 1965.
- [52] K. Kamala Bharathi, G. Markandeyulu, C.V. Ramana, Electrochem. Solid-State Lett. 13 (2010) G98.
- [53] K. Kamala Bharathi, C.V. Ramana, J. Mater. Res. 26 (2011) 584.
- [54] Y.Z. Wang, G.W. Qiao, X.D. Liu, B.Z. Ding, Z.Q. Hu, Mater. Lett. 17 (1993) 152.
- [55] <ftp://download.intel.com/research/silicon/bohr-idf-091603.pdf>, page

CURRICULUM VITAE

Mudavakkat Vikas Haridas was born in Kerala India on August 20th, 1982. He pursued his undergraduate studies at the Sri Jayachamarajendra college of engineering Mysore Karnataka, India, and from the same institution he received his Bachelor of Engineering (B.E) degree in Computer Science and Engineering issued by the Visvesvaraya Technological University 2005.

From September for 2005 to June 2007 he worked in Dubai, United Arab Emirates. During this period, in first job posting he extensively worked on network implementation contracts for SMB to large corporations, Server configuration consultant and hardware support/troubleshooting for server/client environments. His second job posting involved the technical support for enterprise level software and general server hardware consultancy.

In January 2009 he enrolled in the graduate degree program majoring in the Computer Engineering concentration under the Electrical & Computer Engineering department. There he pursued his research into advanced materials for electronics and computing hardware applications under the guidance of Dr. C.V Ramana. His future focus is to shift into the core VLSI job market armed with device fabrication and materials side knowledge acquired through his research endeavors.

Permanent Address:

C/o M.P Haridasan,
Delta Airlines,
Sharaf Travels,
Khalid Bin Walid Road,
P.O Box 21593,
Dubai,
U.A.E

This thesis was written by Mudavakkat Vikas Haridas.